

# Global space-time scales for day-to-day variations of daily-minimum and diurnal sea surface temperatures: their distinct spatial distribution and seasonal cycles

Kohtaro Hosoda<sup>1</sup>

Received: 26 January 2015 / Revised: 14 September 2015 / Accepted: 17 September 2015 / Published online: 7 October 2015  
© The Oceanographic Society of Japan and Springer Japan 2015

**Abstract** Spatial and temporal scales of day-to-day sea surface temperature (SST) variation were estimated globally based on the microwave cloud-free SST data. By employing the diurnal correction method of SST using sea surface wind (SSW) and solar shortwave radiation data, the scales of daily-minimum SST and diurnal SST amplitude were independently investigated along with seasonal and regional dependency. The daily-minimum SST showed moderate spatial scales of  $O(150\text{--}400\text{ km})$  and relatively long temporal scales of  $O(3\text{--}4\text{ days})$ . In eddy-rich areas, the small spatial and long temporal scales were found to be associated, which suggests that the sub-mesoscale SST structures could be reproduced by spatial–temporal interpolations. Diurnal SST amplitude, which is strongly affected by air–sea interaction and high activity in the warming seasons, showed extremely long/short scales in the zonal/meridional directions of up to  $1000\text{ km}/O(100\text{--}200\text{ km})$ , and its temporal scales were less than 1 day.

**Keywords** Sea surface temperature · Decorrelation scales · Diurnal correction

---

**Electronic supplementary material** The online version of this article (doi:10.1007/s10872-015-0327-z) contains supplementary material, which is available to authorized users.

---

✉ Kohtaro Hosoda  
hosoda@ocean.caos.tohoku.ac.jp

<sup>1</sup> Center for Atmospheric and Oceanic Studies, Graduate School of Science, Tohoku University, 6-3 Aramaki aza Aoba, Aoba, Sendai 980-8578, Japan

## 1 Introduction

Sea surface temperature (SST) is a fundamentally important parameter in atmospheric and oceanographic research and its application. SST fields are also indicative of the horizontal thermal structure in the ocean surface layer. Monitoring SST frontal structures can provide information about oceanic currents, eddies (de Souza et al. 2006; Dong et al. 2011), and fishing grounds (Zainuddin et al. 2006; Lan et al. 2012). Hosoda et al. (2012) showed that temporal scales of SST fronts range from 10 to 40 days in most parts of the global ocean. Daily measurements are therefore essential in order to monitor and understand the variability of SST fields. Daily-step, high-resolution ( $\leq 0.25^\circ$ ) gridded SST data sets based on satellite remote sensing have been provided in recent years, and often include daily-mean SST fields.

One of the methods widely used for producing high-resolution SST data sets is optimal interpolation (OI). If the objective system is linear and the covariances are correctly specified, then an SST field estimated by OI will be optimal in the sense that the mean square error of the estimates is minimized (Emery and Thomson 2001). Therefore, the covariance functions should be estimated before OI processing. Usually, the covariance functions are approximately given by a few parameters called decorrelation scales, which are determined by least-square fitting of a simple function to the covariances. Calculation of the covariance functions requires that the mean and trend be removed from the data (Emery and Thomson 2001).

Several studies have estimated global space-time scales of SST. Targeting the gyre-scale and annual and interannual signals, White (1995) computed three-dimensional covariance matrices and decorrelation scales of SST and

subsurface temperature using in situ measurements. Reynolds and Smith (1994) and Reynolds et al. (2007) estimated spatial (zonal and meridional) scales of respective SST anomalies, which were defined as the change in SST from the previous output product (weekly or daily interval), using satellite remote sensing and in situ measurements. By applying scale-division to SST variability for remote sensing SST data, Kurihara et al. (2006) derived spatial and temporal scales of SST variation components. They used three spatial wavelengths (small: 50–145 km, medium: 145–690 km, and large:  $\geq 690$  km); and two fluctuation period ranges (short: 27–53 days and long:  $\geq 53$  days). Hosoda and Kawamura (2004) estimated the decorrelation of SST using 1-year Advanced Microwave Scanning Radiometer for EOS (Earth Observing System) (AMSR-E) daily-mean data. The climatological annual cycle of SST at each grid point was removed before deriving the short-term, small-scale SST variability. It was concluded that the spatial and temporal scales of these daily-mean SST anomalies were less than 300 km and 3 days, respectively. The temporal scales that were longer than 2 days were not widely distributed, which suggests that the optimal interpolation for daily-step SST in the temporal direction was not efficient. Seasonal variability of daily-mean SST space-time scales was discussed in Hosoda and Kawamura (2004), but was not addressed by Kurihara et al. (2006) or Reynolds et al. (2007). Hosoda and Kawamura (2004) showed that large spatial and short temporal scales are distributed throughout the summer, while small spatial and long temporal scales are found in the winter.

The diurnal cycle of SST is one of the most dominant signals in short-term SST variability. The period of the diurnal cycle is regulated by the earth's rotation (1 day). It is understood that its amplitude is mostly determined by the local intensity of solar radiation and the local strength of sea surface wind (SSW): sufficiently weak SSW is a necessary condition for causing large diurnal SST warming. Kawai and Wada (2007) documented a review of diurnal SST phenomena and their influences on the atmosphere and ocean, and pointed out that the amplitude of diurnal SST variation was up to 5 °C in extreme cases. The traditional daily-mean satellite SST products are provided by the methods of averaging available SST data within a day in each grid point, or OI with a spatial–temporal window (several grid points and adjacent dates). Then, the diurnal variations are essentially contained in such daily-mean SST data. As a thought experiment, it is assumed that SST change within a day is perfectly known as a continuous observation at all times. Then, the daily-mean SST,  $\overline{\text{SST}}_D$ , is defined by following the equation;

$$\overline{\text{SST}}_D(t, \mathbf{x}) = \frac{1}{\Delta t} \int_{0h,t}^{24h,t} \text{SST}(\tau, t, \mathbf{x}) d\tau, \quad (1)$$

where  $t$  and  $\Delta t$  are a digital count of dates and temporal interval of daily-step product ( $\Delta t = 1$  day),  $\mathbf{x}$  is the spatial coordinate of the determined grid point, and  $\tau$  is the time (0:00–24:00) in the date  $t$ . Introducing daily-minimum SST ( $\text{SST}_{\min}(t)$ ) and diurnal variation of SST in the date ( $\delta\text{SST}(\tau, t) \equiv \text{SST}(\tau, t) - \text{SST}_{\min}(t)$ ), Eq. (1) is expressed as,

$$\overline{\text{SST}}_D(t, \mathbf{x}) = \text{SST}_{\min}(t, \mathbf{x}) + \frac{1}{\Delta t} \int_{0h,t}^{24h,t} \delta\text{SST}(\tau, t, \mathbf{x}) d\tau \quad (2)$$

Assuming that the integral of diurnal SST variation can be normalized by its amplitude [ $\Delta\text{SST}(t)$ ], it is possible to rewrite the daily-mean SST as a two-term, daily-step SST time series as,

$$\overline{\text{SST}}_D(t, \mathbf{x}) = \text{SST}_{\min}(t, \mathbf{x}) + \Delta\text{SST}(t, \mathbf{x}) C_{\delta\text{SST}}, \quad (3)$$

where  $C_{\delta\text{SST}}$  gives the temporal integral of normalized diurnal SST oscillation ( $C_{\delta\text{SST}} \equiv \int \delta\text{SST}(\tau, t, \mathbf{x}) d\tau / (\Delta t \Delta\text{SST})$ ). Usually, daily-mean SST data have been produced as the average of available SST data in the determined date as  $\overline{\text{SST}}_D(t, \mathbf{x}) = N^{-1} \sum_{\tau=\tau_0}^{\tau_N} \text{SST}(\tau, \mathbf{x})$ , where  $N$  is number of available data. It is possible that spatial patterns of satellite data availability cause an artificial SST gradient, which could be improperly regarded as a sharp SST front in the data set (e.g. Fig. 3 of Hosoda 2013). Oceanographic applications such those that monitor currents, eddies, and fisheries, view a foundation SST ( $\text{SST}_{\text{fnd}}$ ), defined as SST free from diurnal variability (Donlon et al. 2007), as a requirement by the users. The previous studies described above that have estimated decorrelation scales for SST were also contaminated by diurnal SST variations. Re-examination of decorrelation scales for daily-step SST data production is required using data without the diurnal SST variation. One solution is to use high frequency data to resolve the SST diurnal cycle. However, satellite observations of SST have not been conducted at such the high frequency. While infrared radiometers on geostationary satellites can provide SST measurements with high temporal resolution ( $\leq 1$  h), the cloud contamination problems can cause anomalously cold SST errors in the infrared SST products (Hu et al. 2009; Hosoda 2011), and make it difficult to discuss the diurnal SST variability with sufficient accuracy. The microwave measurements of SST are free from cloud problems owing to their weak absorption by cloud droplets. However, they are not frequently available for one day at a grid point, since both the number and swaths of microwave radiometers on satellites are limited. It is also worthy to note that heavy rain conditions, such as under tropical cyclones, are obstacles for measuring SST by microwave radiometers.

Using microwave radiometers SST data, Hosoda (2013) developed a diurnal correction method for estimating

SST at 1-m depth at local mean times (LMT) of dawn (LMT6:00) and afternoon (LMT13:00) ( $SST_{LMT6,1m}$  and  $SST_{LMT13,1m}$ ) from other LMT observations. These are the expected daily-minimum and daily-maximum in diurnal SST variation for the corresponding date, respectively. Appendix discusses the suitability of regarding these LMT as representative times for the minimum and maximum SST. The diurnal variability at each grid point was empirically corrected by ancillary satellite observations of SSWs and solar radiations. Both the nighttime and morning observations of SST must be diurnally corrected, as was pointed out by Hosoda (2013). Therefore, the daily-step  $SST_{LMT6,1m}$  data by this method might be a candidate for  $SST_{fld}$ . As shown in Sect. 3.1, the spatial distribution is different between the diurnal SST amplitude distribution and the day-to-day change in daily-minimum SST. Therefore, the use of daily-mean SST data sets makes it impossible to examine daily temporal variation in SST, since day-to-day changes of the diurnal SST variation can modify the daily-step SST fields.

The purpose of this study was to estimate the appropriate decorrelation scales for OI of day-to-day SST variations. The decorrelation scales of  $SST_{LMT6,1m}$  and diurnal SST amplitude data by Hosoda (2013) are calculated first to serve this purpose. The removal process of mean and trend in the  $SST_{LMT6,1m}$  time series is also discussed in this study. The contamination effects of diurnal variation onto estimations of daily-mean SST scales are addressed by deriving the spatial temporal scales of diurnal SST variations using  $SST_{LMT6,1m}$  and  $SST_{LMT13,1m}$ .

## 2 Data

The global, daily gridded ( $0.25^\circ$ ) data of  $SST_{LMT6,1m}$  and  $SST_{LMT13,1m}$  were used for estimating decorrelation scales in this study. Hosoda (2013) provided a description of the method for the diurnal correction of microwave measurements of SST by AMSR-E and Windsat. The SSW data from the microwave radiometers and the solar radiation data from Japan Aerospace Exploration Agency (JAXA)/Earth Observation Research Center JAXA Satellite Monitoring for Environmental Studies (JASMES) and International Satellite Cloud Climatology Project radiative flux data set (ISCCP-FD) data sets were also used for correction. Data free areas due to weather conditions (strong rain or wind) and the narrow swath widths of the microwave radiometers were included in this data set. The diurnal correction was conducted empirically by using the following equation:

$$SST_{LMT_{h,1m}} = c_0 + c_1 SST_{obs} + c_2 \ln(SSW) + c_3 SR^2 + c_4 SR^2 \ln(SSW), \quad (4)$$

where  $SST_{LMT_{h,1m}}$  is the 1-m depth temperature at local mean time  $h$  ( $=6:00$  or  $13:00$ ),  $SR$  is the solar radiation, and  $SST_{obs}$  is the satellite remote-sensing observation of SST at each grid point. The coefficients  $c_0 \sim c_4$  were empirically determined by the co-located match-ups of satellite and in situ measurements. This formula was based on the research on the diurnal SST variations by Kawai and Kawamura (2002). This correction scheme was also applied to evening and nighttime observations, using the preceding date's solar radiation. The validation results based on the in situ measurements around LMT 6:00/13:00 showed that the root-mean-square errors (RMSE) of the estimated  $SST_{LMT6,1m}$  and  $SST_{LMT13,1m}$  were less than  $0.78^\circ\text{C}$ , which was comparable to simultaneous observations made by satellite microwave radiometers. Since the observation times by AMSR-E and Windsat were different, simple daily-composites of SST data from these two sensors could contain artificial patterns due to limited data availability and diurnal contamination. By employing the diurnal correction method, these artificial patterns were kept to a minimum. We used the  $SST_{LMT6,1m}$  and  $SST_{LMT13,1m}$  data from 1 January 2003 to 31 December 2010. The combined use of data from two microwave radiometers provided data coverage in daily composite of more than 85 % in the mid-latitude and low-latitude areas. Therefore, smoothing or interpolation was not introduced before the estimation of decorrelation scales.

For addressing the activity of oceanic mesoscale eddies, we used the eddy kinetic energy (EKE) obtained from Maps of Absolute Dynamic Topography (MADT) and absolute geostrophic velocities by Archiving, Validation and Interpretation of Satellite Oceanographic data (AVISO; Le Traon et al. 1998). The  $EKE = 1/2(u'^2 + v'^2)$  was calculated, where  $u'$  and  $v'$  were the velocity anomalies defined as the difference between the current and the annual mean currents ( $\bar{u}$ ,  $\bar{v}$ ). The AVISO MADT data have been provided as a global projection on a 1/3 Mercator grid. The mean currents and the EKE from 2003 to 2010 were computed at each grid point.

Atmospheric forcing is discussed in relation to the diurnal SST variation. The daily-mean SSW was derived from an AMSR-E and Windsat composite, and the daily-mean solar radiation data by JASMES data (<http://kuroshio.eorc.jaxa.jp/JASMES/index.html>) was used. The spatial grid of these data sets was  $0.25^\circ$ . Air temperature data at 10 m height, sea level pressure (SLP), and the net heat flux (NHF) data were acquired from the atmospheric reanalysis product. The Modern-Era Retrospective-analysis for Research and Applications (MERRA) is one of the latest atmospheric reanalyses produced by the National Aeronautics and Space Administration Goddard Space Flight Center Global Modeling and Assimilation Office, using the Goddard Earth Observing System Data Assimilation

System (Rienecker et al. 2011). One of the MERRA’s characteristics is the spatial resolution of  $1/2^\circ$  latitude  $\times$   $2/3^\circ$  longitude, which is comparable to microwave SST remote sensing data. Note that the effective resolution of microwave SST is regulated by the footprint of the main observing channel for SST (6 GHz), which is  $O(50\text{ km})$  (Kawanishi et al. 2003, <http://www.remss.com/missions/windsat>), although the microwave SST products are generally provided as  $0.25^\circ$  grid data. The temperature differences between SST and air temperature at 10 m height at  $\text{LMT}6:00 \pm 30\text{ min}$  were calculated from the hourly temporal resolution MERRA data. In this study, the temperature difference is defined as positive if the air temperature is higher than the SST. Bicubic interpolation was conducted for interpolating MERRA air temperature data onto microwave SST  $0.25^\circ$  grid point. The mean SLP distribution for each season was calculated for the global oceans over the period from 2003 to 2010. The NHF data at the sea surface was defined as the downward positive form as follows:

$$\text{NHF} = \text{SR}_n^\downarrow + \text{LR}_n^\downarrow - \text{SH}^\uparrow - \text{LH}^\uparrow, \quad (5)$$

where  $\text{SR}_n^\downarrow$  and  $\text{LR}_n^\downarrow$  are the net downward shortwave and longwave radiations at the sea surface, and  $\text{SH}^\uparrow$  and  $\text{LH}^\uparrow$  are the upward sensible and latent heat fluxes. The directions of the fluxes in Eq. (5) were determined by the MERRA product. The intraseasonal intensity of the NHF,  $\text{NHF}_A$ , was obtained at each grid point for every season by the following calculation:

$$\text{NHF}_A^2(\mathbf{x}) = \frac{1}{N-1} \sum_{\text{yr}=2003}^{2010} \sum_d (\text{NHF}(\mathbf{x}, d) - \overline{\text{NHF}}_{\text{yr},A}(\mathbf{x}))^2, \quad (6)$$

where a string  $A$  represents the season calculated [e.g., June, July, and August (JJA) for boreal summer];  $\text{NHF}(\mathbf{x}, d)$  is a NHF value at grid point  $\mathbf{x}$  on date  $d$ , comprising the investigating season indicated by  $A$ ;  $\overline{\text{NHF}}_{\text{yr},A}(\mathbf{x})$  is the average of  $\text{NHF}(\mathbf{x}, d)$  at the grid point in the season  $A$  of year  $\text{yr}$ . The square root of Eq. (6) will be used for discussing the atmospheric contribution to SST variability in Sect. 4.

### 3 Method

#### 3.1 Definition of diurnal SST amplitude

The diurnal variation amplitude of  $\text{SST}_{1\text{m}}$  ( $\Delta\text{SST}$ ) with daily-step interval is defined by the following equation:

$$\Delta\text{SST}(\mathbf{x}, t) = \begin{cases} \text{SST}_{\text{LMT}13,1\text{m}} - \text{SST}_{\text{LMT}6,1\text{m}}, & \text{under condition Eq.(8)} \\ 0 & \text{(otherwise)} \end{cases} \quad (7)$$

$$\text{SST}_{\text{LMT}13,1\text{m}} \geq \text{SST}_{\text{LMT}6,1\text{m}} \quad \& \quad \text{SST}_{\text{LMT}13,1\text{m}} \geq \text{SST}_{\text{LMT}6+24,1\text{m}} \quad (8)$$

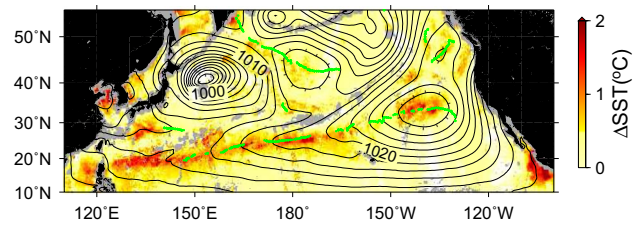


**Fig. 1** An example of diurnal sea surface temperature (SST) amplitude ( $\Delta\text{SST}_{1\text{m}}$ ) on 13 May 2010. Gray areas correspond to the lack of data by the composite of the AMSR-E and Windsat. Contours are the daily-mean sea level pressure (SLP) field obtained the MERRA reanalysis [contour interval (C.I.) = 2 hPa]. Green dots show the position of the atmospheric pressure ridges of the daily-mean SLP

where  $\mathbf{x}$  and  $t$  are the location and date of calculation,  $\text{SST}_{\text{LMT}6+24,1\text{m}}$  is  $\text{SST}_{\text{LMT}6,1\text{m}}$  on the next day. The second condition is included to remove phenomena of SST day-to-day monotonic increases in the discussion about the diurnal variation. Figure 1 shows an example of diurnal SST amplitude defined by Eq. (7) in the North Pacific, on 13 May 2010. The overlaid contours indicate the daily-mean SLP field derived by the MERRA reanalysis. Green dots are the position of the atmospheric pressure ridges over oceans, which were derived as grid points with the following conditions: (1) the sign of SLP spatial gradient ( $\nabla\text{SLP}$ ) was changed along the zonal or meridional direction, (2) laplacian of the SLP ( $\nabla^2\text{SLP}$ ) is negative, and (3) the length along a great circle of the consecutive pressure ridges is longer than 100 km. The high diurnal SST variations were up to  $2^\circ\text{C}$ , especially in the subtropics and Okhotsk Sea. It was found that the high diurnal SST variations frequently co-located with the atmospheric pressure ridges.

Figure 2 illustrates the seasonal variability of  $\Delta\text{SST}$  amplitude, which was defined as its standard deviation (STDV) at each grid point. The calculation was done using  $\Delta\text{SST}$  data from 2003 to 2010. High  $\Delta\text{SST}$  variations were found in the tropical Indo-Pacific Ocean, and during the spring and summer in the mid-latitude oceans. The seasonal change of the high  $\Delta\text{SST}$  area in the tropical Indo-Pacific Oceans corresponds to that of the short-term high SST ( $>30^\circ\text{C}$ ) within the large connected region referred to as Hot Events by Qin et al. (2007). As shown in Fig. 1, it can be seen that at the equator side of the atmospheric high pressure ridges, indicated by dotted lines, high  $\Delta\text{SST}$  variations were found in the mid-latitude oceans. This suggests



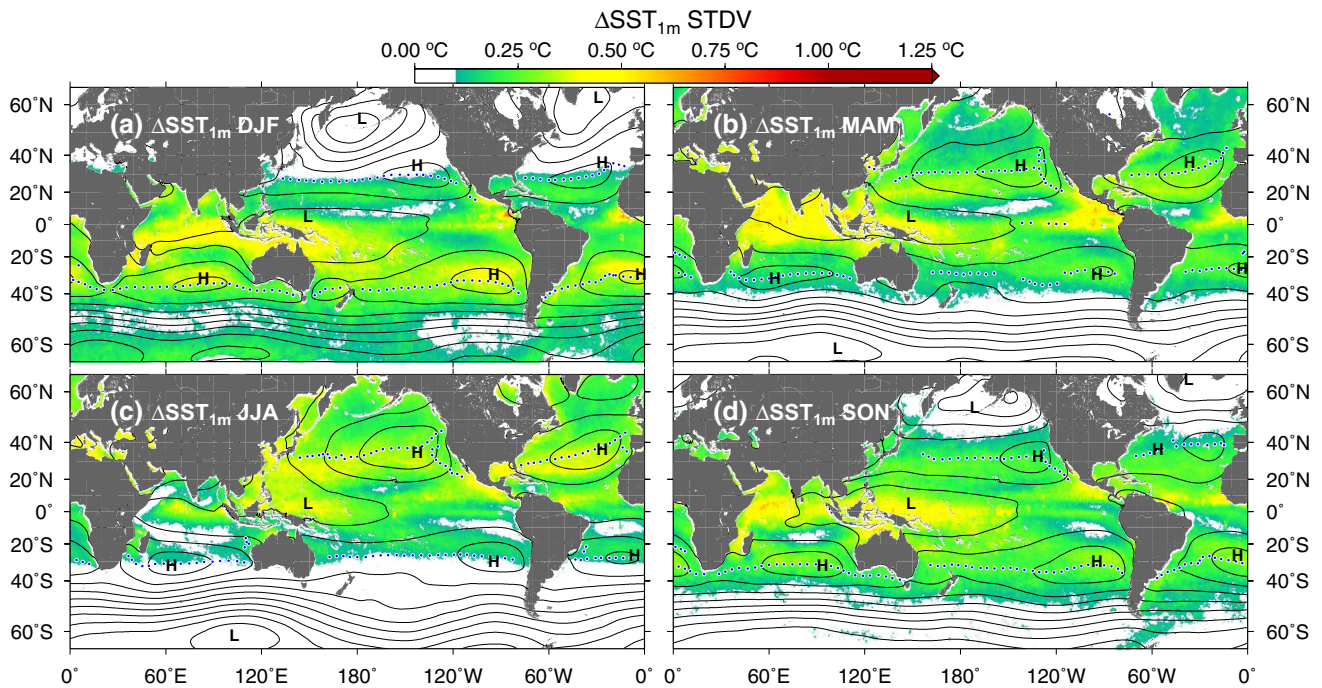


**Fig. 2** Spatial distribution of  $\Delta\text{SST}_{1\text{m}}$  STDV in each season [a December–February, b March–May, c June–August, and d September–November]. The *solid lines* are the contours of seasonal mean sea level pressure (SLP: C.I. = 5 hPa). The *dashed lines*

denote the atmospheric high-pressure ridges of seasonal mean SLP. The estimated values in the *white areas* were less than 0.1 °C. The method for their identification is same as Fig. 1

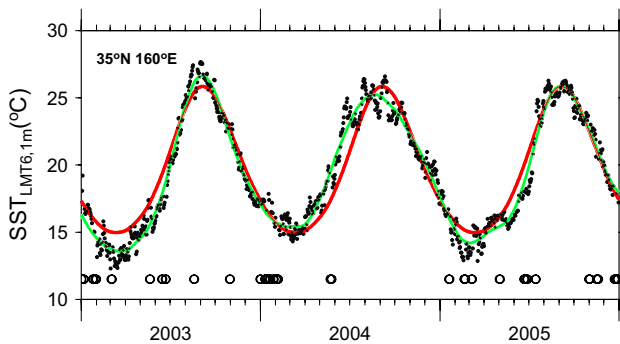


**Fig. 3** An example of  $\text{SST}_{\text{LMT6,1m}}$  and its long-period component time series at 35.0°N, 160°E. The *closed* and *open circles* denote the AMSR-E/Windsat composite of  $\text{SST}_{\text{LMT6,1m}}$  and missing data, respectively. *Red* and *green lines* show the 8-year (2003–2010) averaged annual cycle of  $\text{SST}_{\text{LMT6,1m}}$  and  $\text{SST}_{\text{LMT6,1m}}$  long-period components derived by Eq. (9)

that the calm wind conditions that occur at the weak spatial gradient in SLP are a key factor for generating strong diurnal variations. In the Indian Ocean, the  $\Delta\text{SST}$  variations were not as large in the South Asian summer monsoon seasons (June–August), while wide areas, especially in the Arabian Sea and the Bay of Bengal, had high amounts of active diurnal SST variability in the boreal winter. This feature is consistent with the results of Kennedy et al. (2007),

where 15 years of drifting buoy observations were used to map the diurnal variability.

### 3.2 Definition of $\text{SST}_{\text{LMT6,1m}}$ anomaly

The  $\text{SST}_{\text{LMT6,1m}}$  anomalies ( $\text{SSTA}_{\text{LMT6,1m}}$ ) in this study are defined as the temperature differences compared to the long-period (seasonal and interannual) variations of  $\text{SST}_{\text{LMT6,1m}}$  at each grid point. The long-period variations of  $\text{SST}_{\text{LMT6,1m}}$  were, at each grid point, determined by independent least-squares fitting of a two-frequency (annual and semi-annual), windowed, sinusoidal harmonics curve fitting. Although similar data processing is available by using Morlet wavelet transform and its inverse transform as a band-pass filter (e.g., Hasegawa et al. 2007), one of the advantages by this method is applicability to time series with data gaps. The fitting function is:

$$\text{SST}_{\text{LMT6,1m, long}}(\mathbf{x}, t) = A_a(\mathbf{x}, t) \sin(2\pi t_l/365 + \theta_a(\mathbf{x}, t)) \tag{9a}$$

$$+ A_s(\mathbf{x}, t) \sin(2\pi t_l/182 + \theta_s(\mathbf{x}, t)) \tag{9b}$$

where  $t_l$  is the temporal lag (unit: day) from the consideration date. Note that the amplitudes ( $A_a$  and  $A_s$ ) and phases ( $\theta_a$  and  $\theta_s$ ) are given as functions of date  $t$ , as well as the spatial position  $\mathbf{x}$ . Therefore, the amplitudes and phases are

able to be modulated within a year. The fitting process of the two orthogonal functions [Eqs. (9a) and (9b)] was conducted in a gradual manner, as follows:

1. The time series of  $SST_{LMT6,1m}(t)$  with data gaps was extracted at the determined grid point  $\mathbf{x}$ .
2. A consideration date  $t_0$  is determined.
3. The time series of  $SST_{LMT6,1m}(t)$  with length of 365 days ( $t_0 \pm 182$  days) was extracted.
4. Windowed harmonics of annual cycle [Eq. (9a)] were fitted to all the available  $SST_{LMT6,1m}(t)$  data within the 365 days around the consideration date  $t_0$ . Amplitude  $A_a(\mathbf{x}, t_0)$  and phase  $\theta_a(\mathbf{x}, t_0)$  for the annual harmonics around the consideration date  $t_0$  are given.
5. The  $SST_{LMT6,1m}(t)$  residual derived from the windowed annual harmonics was calculated [Eq. (9a)], and the time series of the residual time series with length of 183 days ( $t_0 \pm 91$  days) was extracted.
6. Windowed harmonics of semi-annual cycle [Eq. (9b)] were fitted to all the available  $SST_{LMT6,1m}(t)$  residual derived from windowed annual harmonics within the 183 days around the consideration date  $t_0$ .

Amplitude  $A_s(\mathbf{x}, t_0)$  and phase  $\theta_s(\mathbf{x}, t_0)$  for the semi-annual harmonics around the consideration date  $t_0$  are given.

Then, for the next date ( $t_0 + 1$ ), the same windowed annual/semi-annual harmonics fittings were conducted for  $SST_{LMT6,1m}(t)$  time series in the period of  $t_0 + 1 \pm 182$  days/ $t_0 + 1 \pm 91$  days, respectively. This method corresponds to the Morlet wavelet filter with setting of high temporal and low frequency resolutions, which enables the filter to include the interannual signal as the modulation of amplitudes and phases. The semi-annual component in Eq. (9) was introduced to address the asymmetry of long cold seasons and short hot summers, especially in the high-latitude oceans (Provost et al. 1992). Using long-term in situ SST, atmospheric temperature, and SLP data from the monthly Comprehensive Ocean-Atmosphere Data Set (COADS), Yashayaev and Zveryaev (2001) demonstrated that a combination of annual and semi-annual harmonics accounts for more than 95 % of the seasonal variability.

An example for the spatial grid point (35.0°N, 160°E) is shown in Fig. 3. The closed and open circles denote the raw  $SST_{LMT6,1m}$  time series and dates of missing data, respectively. The 8-year (2003–2010) averaged annual cycle of  $SST_{LMT6,1m}$  at this point is given by a red line. The interannual variability, such as amplification (winter and summer in 2003), phase shift (spring to summer in 2004), and phase change (early spring in 2005) of the annual cycle, is not followed by the 8-year-mean annual cycle. In the method used by Hosoda and Kawamura (2004), the interannual

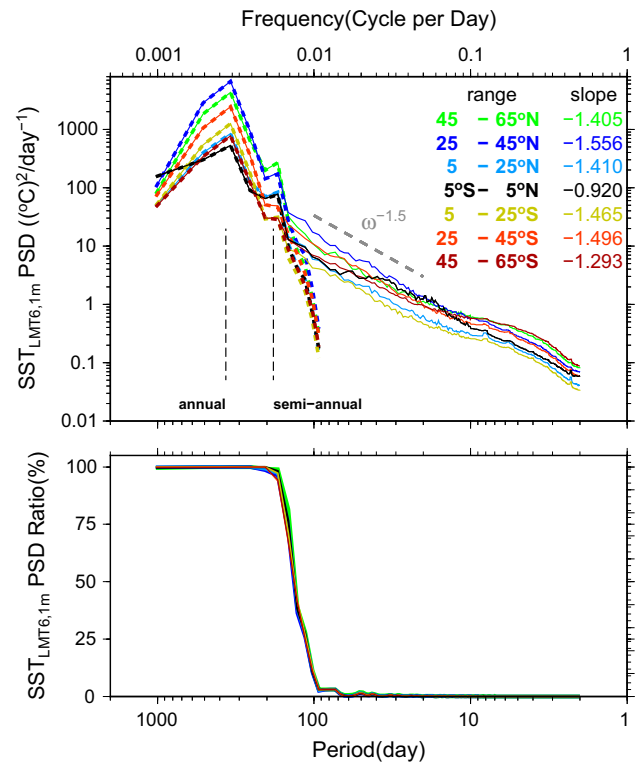


**Fig. 4** (Upper) ensemble mean frequency spectra of  $SST_{LMT6,1m}$  (solid lines) and  $SST_{LMT6,1m}$  long-period component (dashed lines). (Lower) percentage (%) of the ensemble mean frequency spectra between long-period and raw  $SST_{LMT6,1m}$ . The long-period components were obtained from windowed, sinusoidal harmonics curve fitting using Eq. (9). The latitudinal band width for averaging is  $10^\circ$  for tropic oceans and  $20^\circ$  for extra-tropical oceans. The slopes of frequency spectra shown in the upper right corner are derived from least-square fitting of linear function in the range of 20–100-day period. Two dashed lines mark positions of annual (365-day period) and semi-annual (182-day period) periods

variability was regarded as SST anomalies, which could cause errors for decorrelation scale estimation. The least-squares fitting for this point is illustrated by a solid green line. The interannual variability, such as that listed above, was involved in this long-period smoothing.

The upper panel of Fig. 4 shows the latitudinal dependence of ensemble mean frequency spectra of the long-period components and raw  $SST_{LMT6,1m}$  time series. The calculations were conducted by using the AMSR-E/Windsat composite time series of  $SST_{LMT6,1m, \text{long}}$  and  $SST_{LMT6,1m}$ , respectively. For the latter, points with missing  $SST_{LMT6,1m}$  observations were filled by the long-period smoothing at their corresponding dates. The long-period and raw frequency spectra at each grid point were calculated by  $SST_{LMT6,1m, \text{long}}$  and  $SST_{LMT6,1m}$  data from 2003 to 2010, for global oceans without sea-ice cover. Then, the frequency spectra were averaged in a zonal  $10^\circ$  band ( $5^\circ\text{S}$ – $5^\circ\text{N}$ ) in tropical oceans, and  $20^\circ$  bands for subtropical and

subarctic oceans. Annual signals were prominent in the mid latitudes (25–45°S) in the Southern Hemisphere, and the mid (25–45°N) and high (45–65°N) latitudes in the Northern Hemisphere. Semi-annual components were clearly found in the Northern Hemisphere and tropics, while those in the Southern Hemisphere were weak. As shown in Lower panel of Fig. 4, the spectral intensities over 160 day period [ $\omega < 0.006$  cycle per day (cpd)] of the low-pass filtered SST data were more than 95 % of the original raw SST spectra. Half-power points were found around 130-day period (0.0076 cpd). This suggests that the long-period component (semi-annual to interannual periods) in the original raw SST data could be sufficiently reproduced in the long-period smoothing. The spectral intensities of long-period components [Eq. (9)] are significantly smaller in the frequency range of less than 100 days ( $\omega > 0.01$  cpd). Using AMSR-E SST and atmospheric reanalysis data in the extratropical North Pacific, Hosoda (2012) pointed out that SST changes in the weekly to intraseasonal scales (periods less than 100 days ( $\omega > 0.01$  cpd) were mainly dominated by NHF, while a part of the perturbations in the intra-annual period (100–200 days:  $\omega = 0.01 - 0.005$  cpd) suggests that the ocean disturbances would drive air–sea interactions. This suggests that the scale division around the 100-day period, which could be implemented by the long-period smoothing using Eq. (9), is a reasonable reproduction of the realistic SST variability. No significant spectral gap or peak was found in this frequency range, which suggests that an additional scale-division would be unnecessary for deriving decorrelation scales. In the weekly-to-biweekly range ( $\leq$  about 15–20 days period: 0.06–0.05 cpd), weak spectral bulges were found in the mid-latitude and high-latitude areas, which would be generated by eastward propagation of the traveling anticyclone/cyclone in the Westerlies. For avoiding contamination from this characteristic oscillation, frequency spectral slopes in the range of 20–100 days period (0.05–0.01 cpd) were calculated. They have around  $O(\omega^{-1.5})$ , except for tropics and high latitudes in the Southern Hemisphere (45–65°S), where the spectral intensities of the annual cycle are the lowest and the second minimum. In the tropics, a broad peak of spectral intensity is found in this frequency range, owing to the Madden–Julian oscillation (MJO) with temporal scales of  $O(30-90$  days).

An  $SST_{LMT6,1m}$  anomaly ( $SSTA_{LMT6,1m}$ ) in this study is defined as the difference between the observed  $SST_{LMT6,1m}$  and the long-period component  $SST_{LMT6,1m,long}$ , as

$$SSTA_{LMT6,1m} \equiv SST_{LMT6,1m} - SST_{LMT6,1m,long}. \quad (10)$$

The decorrelation scales obtained and reported in this paper are applied to only  $\Delta SST$  and  $SSTA_{LMT6,1m}$ . The decorrelation scales for  $SST_{LMT6,1m,long}$  are not obtained. This is because the long-period component  $SST_{LMT6,1m,long}$  can

be filled by temporal interpolation at each grid point without spatial smoothing. From examples of fields from long-period component  $SST_{LMT6,1m,long}$  and the  $SSTA_{LMT6,1m}$  (figure not shown), it is found that nearly steady currents, and mesoscale oceanic disturbances, such as eddies and meanders, were reproduced in the long-period component. On the other hand, the  $SSTA_{LMT6,1m}$  fields contained the deformation of mesoscale oceanic structures, generation of eddies (i.e., sub-mesoscale phenomena in oceans), and perturbations via air–sea interactions under atmospheric weather disturbance.

Figure 5 shows the spatial distribution of  $SSTA_{LMT6,1m}$  STDV. The spatial distribution of  $SSTA_{LMT6,1m}$  is distinctly different from that of the  $\Delta SST$ : these are inseparably intermixed in the daily-mean SST data sets. Large  $SSTA_{LMT6,1m}$  amplitudes are also found in the western boundary current regions (e.g., Mixed Water Region, the Gulf Stream, Agulhas Current, and the Brazil–Malvinus Current), which are clearly seen in colder seasons, as with the hot seasons. This is in contrast with the cases of  $\Delta SST$ . In warm seasons (spring and summer), high variations of  $SSTA_{LMT6,1m}$  are distributed widely in the mid-latitude and high-latitude areas, especially on the polar sides of the atmospheric high-pressure ridges. This is significantly different from the  $\Delta SST$  distribution shown in Fig. 2. Overlaid contours in Fig. 5 indicate the activity of intra-seasonal NHF in each season. The large  $SSTA_{LMT6,1m}$  STDV areas correspond to the those with large intra-seasonal NHF. The sensitivity of  $SSTA_{LMT6,1m}$  to the NHF magnitude is higher in the warm seasons, because the mixed layer is shallower in these periods due to solar heating. High  $SSTA_{LMT6,1m}$  activity areas are also found in the upwelling areas, which include the equatorial upwelling area in the Pacific and coastal upwelling areas such as the Costa Rica Dome.

### 3.3 Estimation of $SSTA_{LMT6,1m}$ and $\Delta SST$ decorrelation scales

The monthly mean correlation matrices of  $SSTA_{LMT6,1m}$  and  $\Delta SST$  are given as a three dimensional function of  $\mathbf{x}_l = (x_l, y_l, t_l)$ , where  $x_l$ ,  $y_l$ , and  $t_l$  are, respectively, the zonal, meridional, and temporal relative distances from the center grid point. The correlation matrix of  $SSTA_{LMT6,1m}$  ( $\Delta SST$ ) at each grid point was calculated with the size of  $|x_l| \leq 15^\circ$ ,  $|y_l| \leq 7.5^\circ$ ,  $|t_l| \leq 15$  days ( $|x_l| \leq 30^\circ$ ,  $|y_l| \leq 15^\circ$ ,  $|t_l| \leq 15$  days). These matrix sizes were determined by a trial and error method. The decorrelation scales of  $SSTA_{LMT6,1m}$  and  $\Delta SST$  were assumed to be anisotropic Gaussian, as

$$\text{corr}(\mathbf{x}, \mathbf{x}_l) = \exp \left( - \left( (x_l/\lambda_x)^2 + (y_l/\lambda_y)^2 + (t_l/\lambda_t)^2 + \varepsilon_0 \right) \right) \quad (11)$$



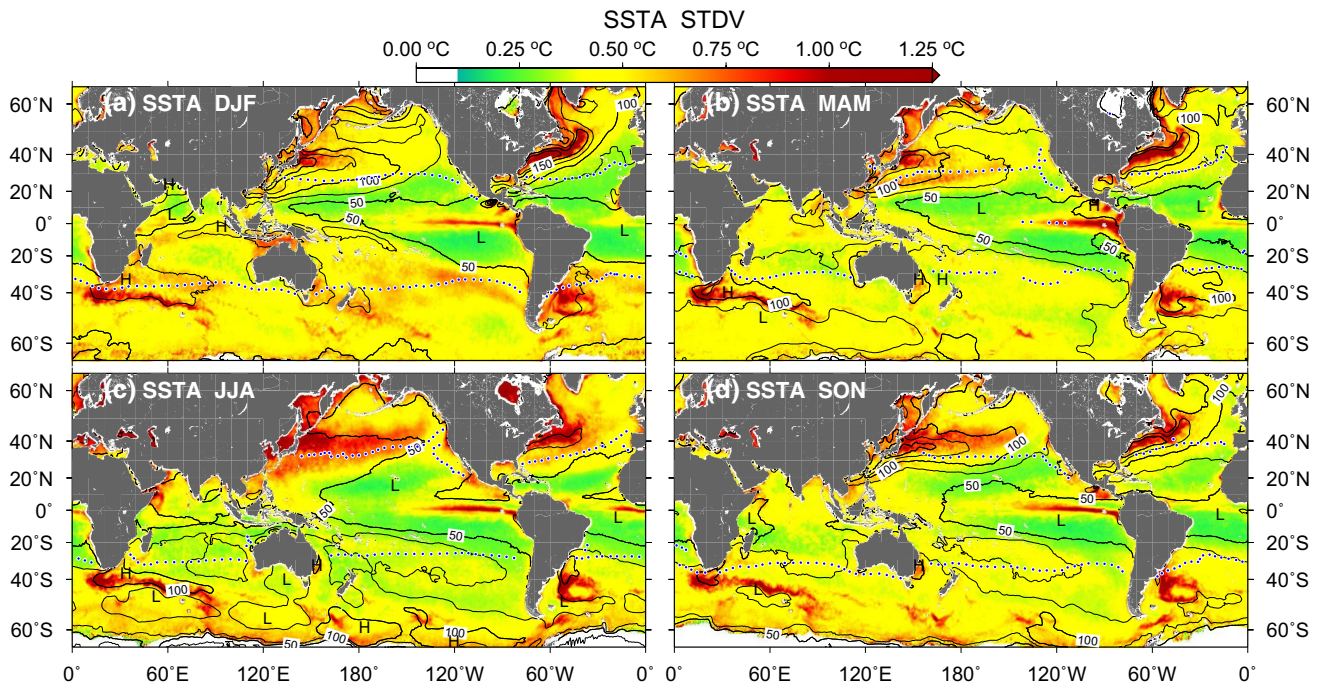


**Fig. 5** Same as Fig. 2, except for the standard deviation of the  $SSTA_{LMT6,1m}$ . The *solid lines* are the contours of the NHF intraseasonal variability calculated by Eq. (6). ( $C.I. = 25 \text{ W/m}^2$ ). The *dashed lines* denote the atmospheric high-pressure ridges of seasonal mean SLP

where  $\lambda_x$ ,  $\lambda_y$  and  $\lambda_t$  are the zonal, meridional and temporal decorrelation scales (defined as  $e$ -folding scale), respectively. The center point of the correlation matrix ( $\mathbf{x}_l = (0, 0, 0)$ ) was excluded in the least-square fitting procedure. A parameter  $\varepsilon_0$  in Eq. (11) was introduced to describe a random noise, or signal-to-noise ratio (SNR) in the data set that was used. Based on the following assumptions, Kuragano and Kamachi (2000) derived the relation between SNR and constant coefficient in correlation matrix. The assumptions are: (1) Mean of the errors at a position for the whole period is assumed to be zero. (2) The error is assumed to be a random noise. The correlation coefficient of the error in a different position is zero, and the coefficients between the error and the true value is also zero. From their derivation,  $SNR = \sqrt{\exp(-\varepsilon)/(1 - \exp(-\varepsilon))}$ ;  $SNR = \sigma^t/\sigma^e$ , where  $\sigma^t$  and  $\sigma^e$  are standard deviation of truth and error, respectively. The standard deviation of error is given by the difference between those of the observation and truth, as  $\sigma_e^2 = \sigma_o^2 - \sigma_t^2$ , where  $\sigma_o$  is the standard deviation of observation. Using estimation error of  $SST_{h,1m}$  ( $h = LMT6$  or  $LMT13$ ) data (Hosoda 2013) as  $\sigma_e$  and global averaged intra-seasonal variability of the  $SSTA_{LMT6,1m}$  and  $\Delta SST$  (Figs. 5 and 2) as  $\sigma_o$ , the constant coefficients  $\varepsilon$  were globally set to 0.1/0.3 for daily-minimum/diurnal SST amplitude, respectively. The scales are derived for each grid point ( $0.25^\circ \times 0.25^\circ$ ) with a monthly-step interval. This form of least squares fitting is based on SSH scale estimation by Kuragano and Kamachi (2000) and SST

scale estimation by Hosoda and Kawamura (2004) and Kurihara et al. (2006).

Note that the temporal decorrelation scales for  $\Delta SST$  was obtained from a daily-step data set. This study does not focus on a decaying time scale (about a few hours) of diurnal SST variation in one day. If the longer temporal scale of daily-step  $\Delta SST$  was obtained at a grid point, it means that the diurnal SST amplitudes were persistent in successive dates at the same grid point, and temporal interpolation is capable of filling gaps by data at adjacent dates.

The microwave SST data ( $SSTA_{LMT6,1m}$  and  $\Delta SST$ ) used in this study have gaps in the daily-step fields. By combination use of AMSR-E and Windsat, the coverage of microwave SST data is up to 85 %, even in the mid and low latitudes (Hosoda 2013). The spatio-temporal smoothing or OI using a priori decorrelation scales for fulfilling the data gaps were not adopted, since such smoothing could affect the derived results in this study by removing small-scale phenomena in spatial and temporal directions. Therefore, ensemble variance/covariances for the 8-year period are conducted under an ergodic hypothesis, in which computed statistics as a function of the specific relative distance  $\mathbf{x}_l$  are assumed to be equivalent to those from data of independent realizations of the same process for different cases. Based on this hypothesis, the variance/covariance of microwave SST data with  $\mathbf{x}_l$  were calculated by summation of data at different time square-sums/product-sums of all of available data at a specific month in 2003–2010. The calculations of



variance/covariance were applied to all  $\mathbf{x}_j$ s, and a filled (i.e., no-gap over ocean grid points) correlation matrix  $\text{corr}(\mathbf{x}, \mathbf{x}_j)$  at the determined grid point  $\mathbf{x}$  for the specific month was obtained from calculated variances and covariances. The similar strategy for obtaining ensemble variance/covariance was adopted by White (1995) and Kuragano and Kamachi (2000). As discussed later, since geographical discrepancy in the decorrelation scales is found within a small distance, ensemble variance/covariance are not calculated as spatial averaging of them in low-resolution spatial grid size.

Another disadvantage of microwave SST data is the coastal mask, which is caused by the microwave radiometers' large footprint [ $O(50 \text{ km})$ ]. In this study, the decorrelation scales in coastal area (distance from coastline  $<50 \text{ km}$ ) were not calculated. In the near-coastal areas, the least-square fitting was applied to the three-dimensional correlation matrix for the grid points where the data were available. If the grids at which the width of lands between the grid point and the center of matrix was over  $40 \text{ km}$ , the correlations at the grids were excluded for the fitting. If the number of the available grid points was less than 10, the calculation was not operated. In these areas, it is necessary to evaluate these statistics by using high resolution and highly quality-controlled infrared SST data, in which the cloud contamination errors are carefully eliminated. This aspect will be addressed in future studies.

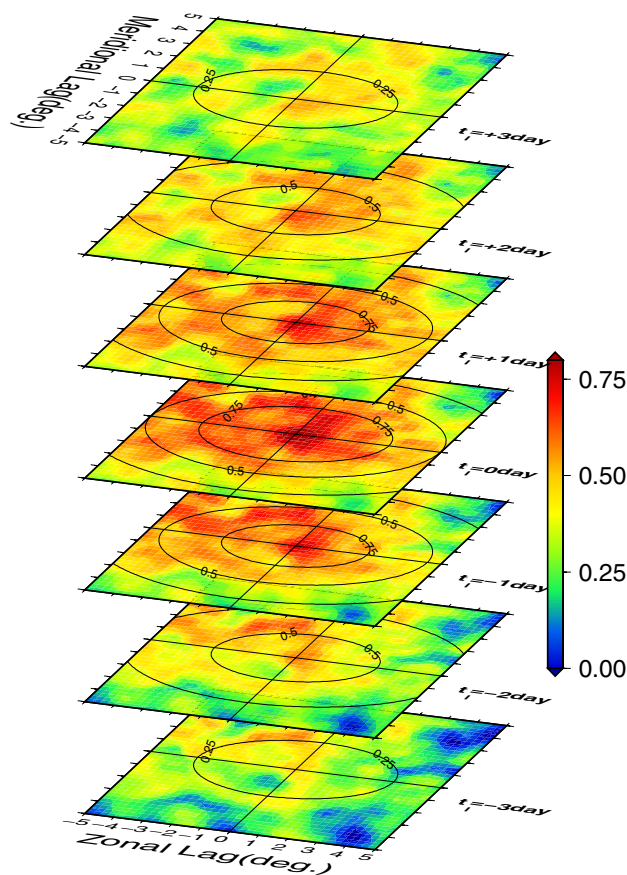
Calculation of  $\Delta\text{SST}$  scales are conducted if the following conditions are satisfied at the consideration grid point: (1) RMSD of  $\Delta\text{SST}$  on each month at the grid point is larger than  $0.1 \text{ }^\circ\text{C}$ , and (2) number of dates with  $\Delta\text{SST} > 0.5 \text{ }^\circ\text{C}$  is larger than 30 days. These conditions were adopted for removing artificial longer scales, which are derived if the significant diurnal variations are not observed in a large spatial area or long temporal period.

Figure 6 presents an example of the correlation matrix of  $\text{SSTA}_{\text{LMT6},1\text{m}}$  at  $35^\circ\text{N}$ ,  $180^\circ$  for March. This calculation was obtained from the  $\text{SSTA}_{\text{LMT6},1\text{m}}$  in the spatial range of  $165^\circ\text{E}$ – $165^\circ\text{W}$ ,  $27.5$ – $42.5^\circ\text{N}$ , and in the period from 13 February to 16 April. In this spatio-temporal space, the center points for the correlation matrix were specified at  $35^\circ\text{N}$ ,  $180^\circ$ , for the days of March. The derived decorrelation scales  $\lambda_x$ ,  $\lambda_y$ , and  $\lambda_t$  at this point in May, indicated by contour lines in Fig. 6, are  $575.6$ ,  $420.7 \text{ km}$ , and  $5.8$  days, respectively.

## 4 Results

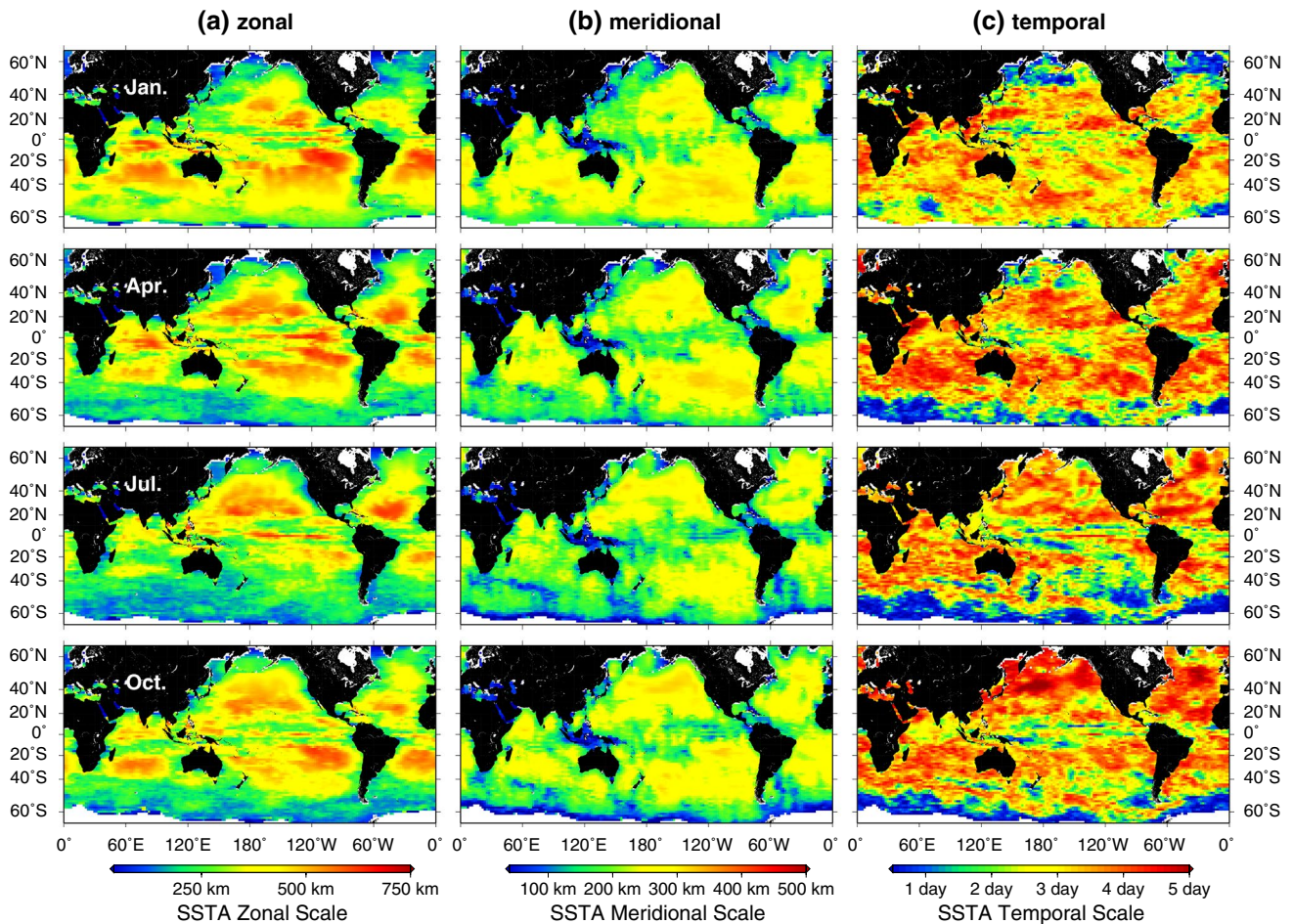
### 4.1 Decorrelation scales of $\text{SSTA}_{\text{LMT6},1\text{m}}$

Figure 7 shows the spatial distribution of the derived  $\text{SSTA}_{\text{LMT6},1\text{m}}$  scales for representative months of each season. The spatial distributions of  $\text{SSTA}_{\text{LMT6},1\text{m}}$  scales for



**Fig. 6** An example of three-dimensional correlation matrix and Gaussian fit for  $\text{SSTA}_{\text{LMT6},1\text{m}}$ , at  $35^\circ\text{N}$ ,  $180^\circ$  for March. The color denotes the correlation coefficient in three-dimensional  $(\mathbf{x}, t)$  space. The solid lines are the contours of least-square fitting of three-dimensional Gaussian by Eq. (11) [C.I. = 0.25 (non-dimension)]

all months are electronically distributed by supplementary materials Figs. S.1–S.12. Long zonal scales, which are up to  $650 \text{ km}$  at the South Pacific off the Peru in January, were found in the various oceans far from continents. The zonal scales in the near-coastal areas are relatively short compared to those at the central ocean basins. The meridional scales are shorter than  $350 \text{ km}$ . The latitudinal variation of oblateness ( $f \equiv 1 - \lambda_y/\lambda_x$ ) is presented in Fig. 8. Large oblateness, or zonal scales that are much larger than meridional ones, are found in the tropics, especially in the Maritime Continent. In the high-latitude oceans, the major part of the scale has small ellipticity. In comparison, the spatial scales derived from day-to-day SST change by Reynolds et al. (2007) are not very anisotropic even in the tropics. A distinctive distribution of the spatial scales in the tropics derived in this study is a drastic change of zonal scales in the latitudinal direction. At the equator, the zonal scales are as long as  $O(400\text{--}500 \text{ km})$ . Alternatively, we can see zonally small scales just off the equator (e.g.,  $200\text{--}300 \text{ km}$  at  $2\text{--}5^\circ\text{N}$  in the central and eastern Pacific), where the tropical



**Fig. 7** Spatial (zonal and meridional) and temporal scales derived from  $SSTA_{LMT6,1m}$  in the representative month of each season (i.e., January, April, July, and October). Note that the different color scales are used for zonal and meridional scales, for emphasizing variability in each scale

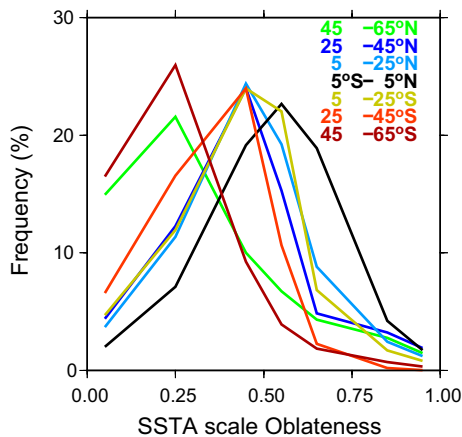


**Fig. 8** Frequency diagrams of latitudinal summation of  $SSTA_{LMT6,1m}$  oblateness. The latitudinal band width for the summation is  $10^\circ$  for tropic and  $20^\circ$  for extra-tropical oceans. Frequency is calculated in each 0.1 bin

instability waves with shorter spatial scale impact on SST (Chelton et al. 2000). This means that the SST decorrelation scales are highly dependent on geographical position. It also suggests that spatial averaging of variance/covariance within large areas might be inappropriate for reproducing realistic SST fields within OI schemes.

In general, the temporal scales are  $O(3-5 \text{ days})$ , in which a significant seasonal change was not found over the majority of global oceans. An exception is the high-latitude Southern Oceans ( $50-60^\circ\text{S}$ ), where the temporal scale in winter is shorter than 2 days. The storm track activity with a short time scale that was associated with the polar jet stream in the Southern Hemisphere extends farther in the winter (Trenberth 1991). It is possible that this high-frequency atmospheric perturbation drives the short-term SST fluctuations in the Southern Ocean. Temporal scales derived from daily-mean  $SSTA_{LMT6,1m}$  by Hosoda and Kawamura (2004) were up to 2 days. Shorter time scales

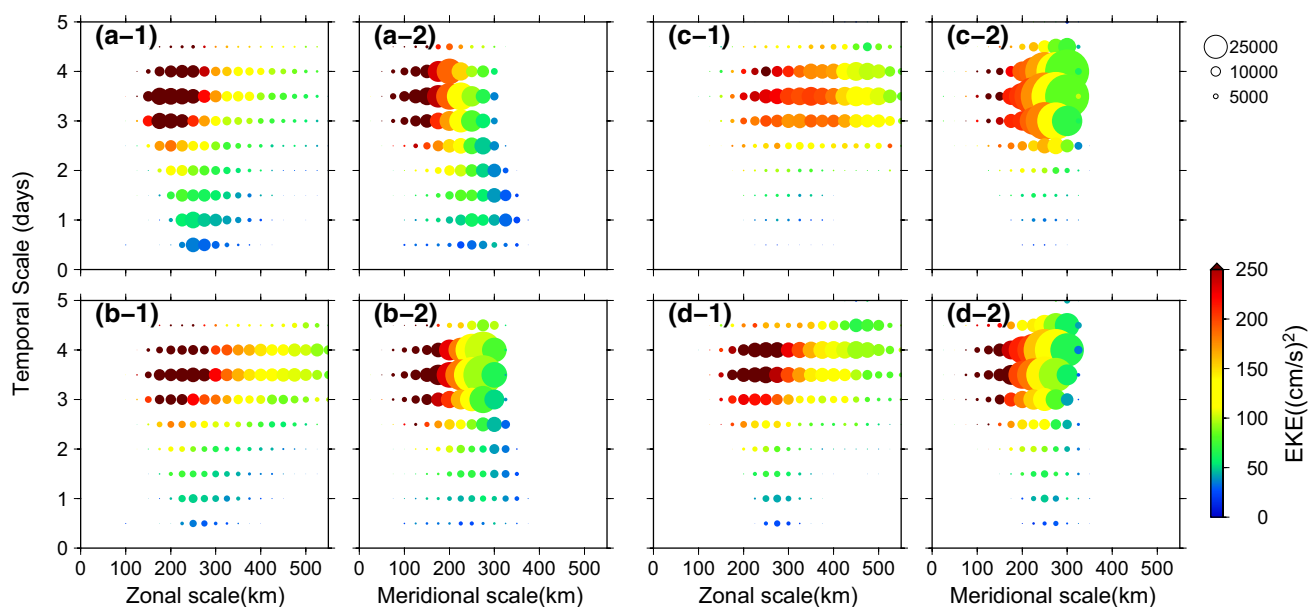


**Fig. 9** Frequency and mean eddy kinetic energy (EKE) on the spatial [zonal (1) and meridional (2)] and temporal scale derived from  $SSTA_{LMT6,1m}$ . Color denotes the mean EKE in  $25 \text{ km} \times 0.5 \text{ days}$  of the  $SSTA_{LMT6,1m}$  scale boxes, and the size of the circle denotes the frequency of the events. **a** winter [December–February in the North-

ern Hemisphere (N.H.,  $20\text{--}60^\circ\text{N}$ ), and June–August in the Southern Hemisphere (S.H.,  $20\text{--}60^\circ\text{S}$ ), **b** spring (March–May in the N.H., and September–November in the S.H.), **c** summer (June–August in the N.H., and December–February in the S.H.), and **d** autumn (September–November in the N.H., and March–May in the S.H.)

of daily-mean SST were found in the summer. By contrast, the temporal scales derived here using daily-minimum SST show that the perturbations with time scales of less than 1 week are dominant in almost all the seasons. The influence of the diurnal SST variations, which contaminated the previous estimation (Hosoda and Kawamura 2004), will be discussed in Sect. 5.

From Fig. 7, the  $SSTA_{LMT6,1m}$  scales in the western boundary current areas (e.g., Kuroshio, Agulhas Current, and Gulf Stream) have a spatially small scale with a long time scale, especially in wintertime. Since the mesoscale eddies are frequently observed in these areas, it suggests that the derived scales are associated with oceanic eddy activity. The variability in the oceans (eddies, meanders, and their deformations/propagations) compared to atmospheric disturbances, has smaller/slower motions. If the  $SSTA_{LMT6,1m}$  variations are largely dominated by propagation of quasi-stable mesoscale eddies or recirculation gyre in the oceanic surface layer (about several hundred meters depth), it is expected that the spatial/temporal scales would be  $O(100\text{--}150 \text{ km})/O(>60 \text{ days})$  in the subtropical oceans, which were derived as the SSH decorrelation scales by Kuragano and Kamachi (2000). On the other hand, the sub-mesoscale phenomena associated with mesoscale variations (e.g., generation, deformation of an eddy, interaction between eddies, and instability of strong currents) has dominant scales of several days. As described in Sect. 3.2, the sub-mesoscale phenomena

are frequently found in the  $SSTA_{LMT6,1m}$  fields. Therefore, the  $SSTA_{LMT6,1m}$  spatial/temporal scales in oceanic eddy-rich areas would be relatively shorter/longer than those in other areas. Figure 9 shows frequency diagrams and mean EKE in the spatial (zonal/meridional) and temporal scale coordinate plane. In this calculation, tropical oceans (area in  $20^\circ\text{S}\text{--}20^\circ\text{N}$ ) were excluded since the EKE was not known in the tropical areas. In winter (Fig. 9(a-1), (a-2): December to February in the Northern Hemisphere and June to August in the Southern Hemisphere), long temporal (3–4 days) and slightly small spatial (200–250 km in zonal, and 100–200 km in meridional directions) scales are associated with the high EKE areas ( $EKE > 300 \text{ (cm/s)}^2$ ). This feature was enhanced in the meridional scale, in which the high mean EKE over  $400 \text{ (cm/s)}^2$  was obtained with a meridional scale of smaller than 100 km. At the short temporal scale ( $< 2 \text{ days}$ ), a low mean EKE of less than  $100 \text{ (cm/s)}^2$  was associated with relatively long spatial scales (250–300 km in zonal and meridional directions). This suggests that the temporally weighted interpolation with small spatial scales would be effective in the eddy-rich areas, while the spatially weighted interpolation with short temporal scales would be appropriate for use with SST data in the eddy inactive area. The mesoscale/sub-mesoscale variability in this area would include oceanic phenomena (e.g., deformation and propagation of mesoscale disturbance) and the modified heat fluxes via change of air–sea



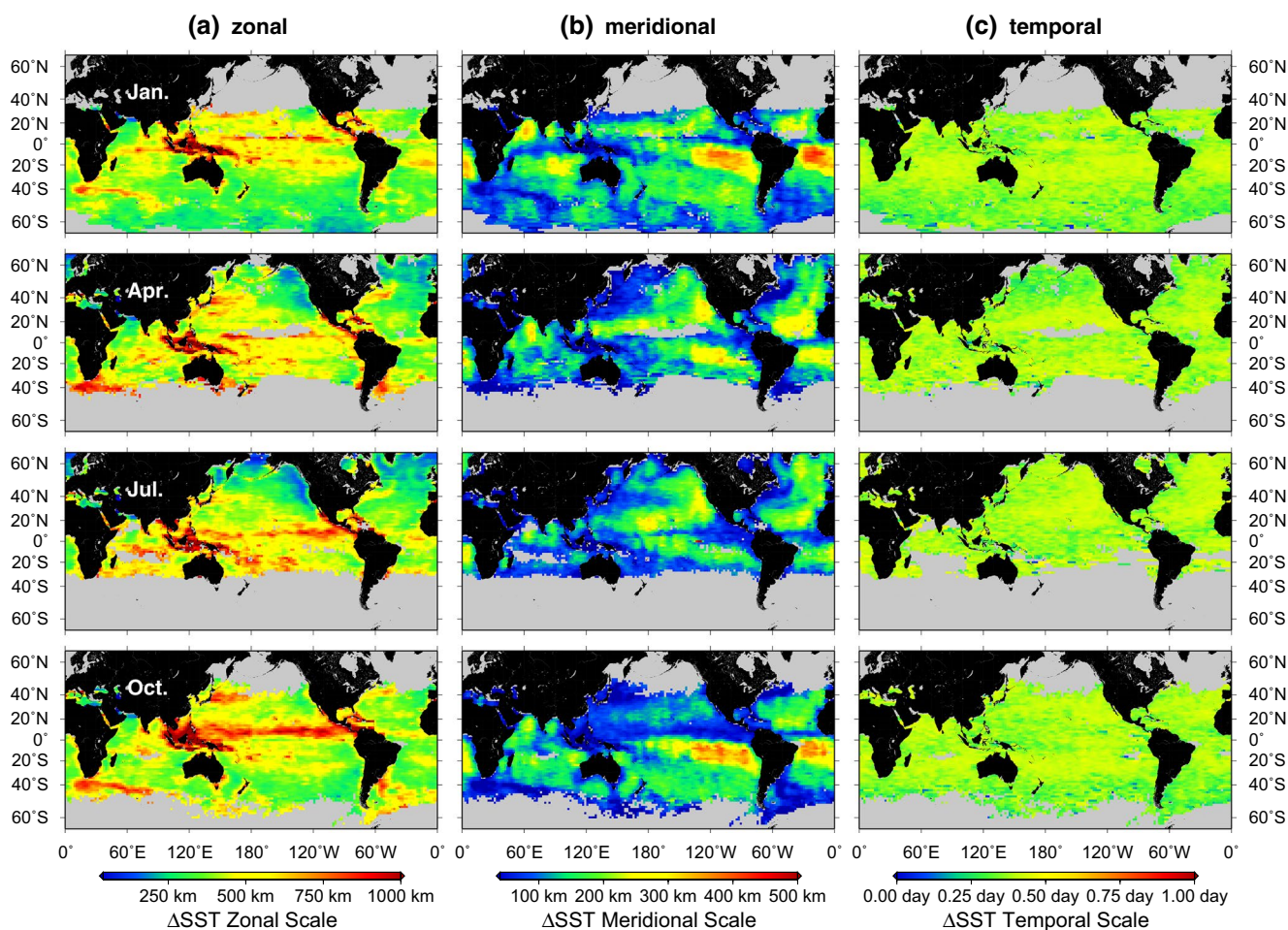


**Fig. 10** Same as Fig. 7, but for  $\Delta$ SST decorrelation scales in the representative month of each season (i.e., January, April, July, and October). Note that the different color scales are used for zonal and meridional scales, for emphasizing variability in each scale

interaction over the warm/cold core eddies (e.g., Sugimoto and Hanawa 2011).

This relationship was also clear in both the spring [Fig. 9(b-1), (b-2): April–June in the Northern Hemisphere and October to December in the Southern Hemisphere] and the autumn [Fig. 9(d-1), (d-2): October–December in the Northern Hemisphere and April to June in the Southern Hemisphere]. Conversely, a weak and obscure relationship was observed in the summer [Fig. 9(c-1), (c-2): July–September in the Northern Hemisphere and January to March in the Southern Hemisphere]. In both eddy active and inactive areas, spatial scales were obtained as more than 300 km in zonal and 200–300 km in meridional, which results in a mean EKE, seen in Fig. 9, that does not have a clear tendency on the spatial–temporal scale plane in summertime.

#### 4.2 Decorrelation scales of $\Delta$ SST

Figure 10 shows the distribution of decorrelation scales derived from  $\Delta$ SST for the representative months of each

season. The spatial distributions of  $\Delta$ SST scales for all months are electronically distributed as supplementary materials Figs. S.13 to S.24. Zonal scales of  $\Delta$ SST up to 1000 km especially in tropics, are close to, or larger than, those from  $SSTA_{LMT6,1m}$ . Long zonal scales were also found at mid latitudes in warming seasons, especially on the colder side of the western boundary currents (Kuroshio Extension, Gulf Stream, Agulhas Retroflexion, and Brazil–Malvinus Confluence Zone). Conversely, the meridional scales of  $\Delta$ SST are  $O(100\text{ km})$  in the majority of oceans, which is much less than that of the  $SSTA_{LMT6,1m}$  meridional scales. This difference causes the high ellipticity for spatial scales of  $\Delta$ SST, which are clearly shown in the latitudinal distributions of oblateness (Fig. 11). The majority of the oblateness is in the range of 0.50–1.00, which means that the zonal scale of  $\Delta$ SST is at least twice as large as the meridional scale at the grid point. An exception is seen at high latitude in the Northern Hemisphere (45–60° N), in which the widths of basins are restricted by large continents.

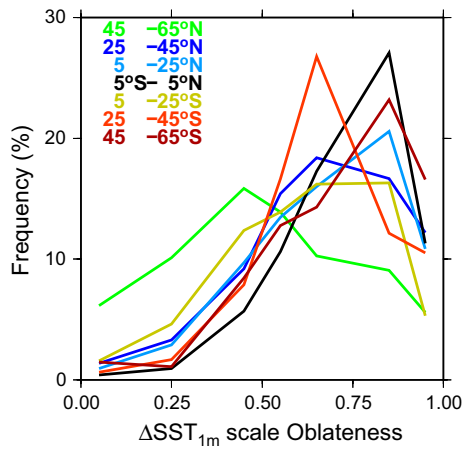


**Fig. 11** Same as Fig. 8, but for  $\Delta$ SST oblateness

Band structure is not clearly observed in the  $\Delta$ SST zonal scales, in contrast to the zonal scales of  $SSTA_{LMT6,1m}$ . Meanwhile, a clear band structure forms the meridional  $\Delta$ SST scales, where the short spatial scales are located at the Intertropical Convergence Zone (ITCZ). It is reasonable to conclude that diurnal heating, which is driven by strong solar radiation and weak winds, is divided at the ITCZ, where the solar radiation is blocked by thick clouds.

Long meridional scales [ $O(200\text{--}300\text{ km})$ ] are found in the spring and summer seasons in the North and South Pacific, and Southern Atlantic. These oceans correspond to the eastern subtropical high SLP areas enhanced by the local monsoon systems (the North American monsoon, the South American monsoon, and the South African monsoon; WCRP The Global Monsoon Systems, available from <http://www.wcrp-climate.org/documents/>

[monsoon\\_factsheet](#)). The subtropical monsoon heating over the continents induces the Rossby wave response to the west, interacting with the mid-latitude westerlies and producing a region of adiabatic descent (Rodwell and Hoskins 2001). The coherent variation of diurnal SST amplitudes in the meridional direction could be generated by the land-air-sea interactions in these regions.

Temporal scales of  $\Delta$ SST are less than 1 day, and a significant seasonal change is not observed. The majority of seasonal changes in  $\Delta$ SST spatial scales are also weak. Zonal scales in the tropics are  $O(500\text{--}600\text{ km})$ , with  $O(100\text{--}150\text{ km})$  meridional scales throughout a year. Long meridional scales of  $O(150\text{--}200\text{ km})$  are found in the low and mid latitudes ( $10\text{--}30^\circ$  in both hemispheres), and shorten in the cooling season to around 120 km. Seasonal changes in high latitude oceans ( $40\text{--}70^\circ$  in both hemispheres) are clearly found, in which long zonal and extremely short meridional scales are derived in winter.

Further analysis of the composite of  $\Delta$ SST extreme cases illustrates why the temporal scale of  $\Delta$ SST is so short. Figure 12 shows the time series composite of several geophysical parameters, in which the center dates (Day Lag = 0) are extracted under the condition of  $\Delta$ SST  $\geq 2.0^\circ\text{C}$  in warming-up periods ( $\partial_t SSTA_{LMT6,1m, long} > 0$ ). The calculation of these composites was conducted using global daily-step data from 2003 to 2010. At the Day Lag = 0, the solar radiation and SSW take their highest and lowest values, respectively. A drastic change (from  $O(4\text{--}6\text{ m/s})$  to less than  $2\text{ m/s}$ ) is seen in the SSW composite, while the change of solar radiation (around  $250\text{--}270\text{ W/m}^2$  to  $312\text{ W/m}^2$ ) is less than 25%. The SSW had gradually been weakened over the preceding several days before the large  $\Delta$ SST event.  $SSTA_{LMT6,1m}$  has a rapid

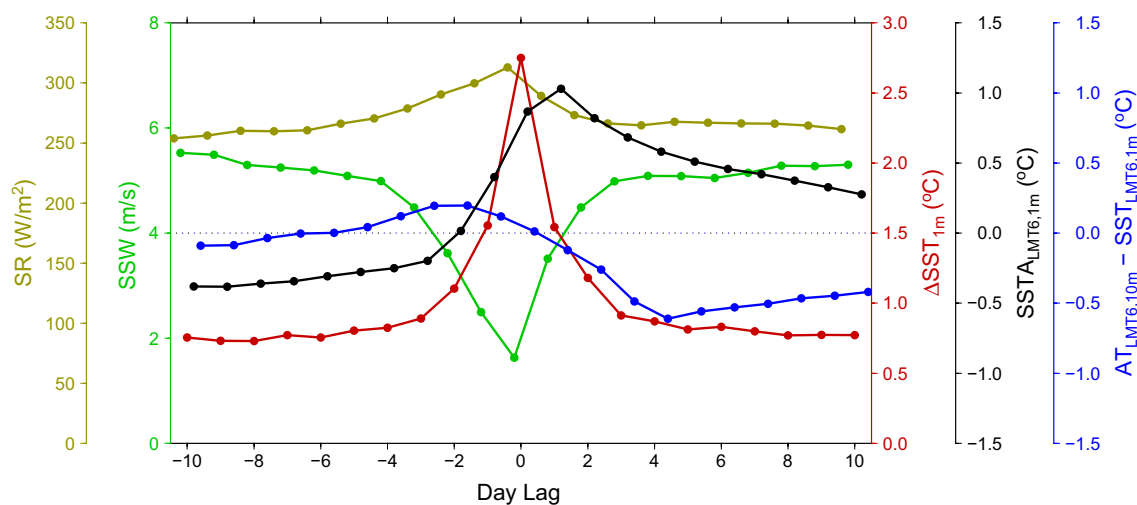


**Fig. 12** Time series composites of the geophysical parameters around the dates (Day Lag = 0 day) with the large diurnal sea surface temperature ranges ( $\Delta$ SST  $\geq 2^\circ\text{C}$ : Red). Green sea surface wind

(SSW), Dark yellow shortwave radiation, Black daily-minimum SST anomaly ( $SSTA_{LMT6,1m}$ ), and Blue air-sea temperature difference at local mean time 6:00 (air temperature at 10 m height— $SSTA_{LMT6,1m}$ )

**Table 1** Summary of the obtained spatial and temporal scales of day-to-day changes of SST parameters

	Daily-min. SSTA	Diurnal SST amplitude	Daily-mean SST
Zonal scale	150–400 km (up to 500 km)	300–500 km (up to 1000 km)	150–300 km
Meridional scale	150–200 km	100–200 km	120–200 km
Temporal scale	3–4 days No significant seasonal change	<1 day	<1–2 days (up to 3 days) Shorter in summer
Amplitude	0.25–1.25 °C	0.0–1.0 °C Active in summer	N/A

Scales and amplitudes of daily-minimum SST and diurnal SST are representative of this study's analysis. For reference, scales derived from daily-mean SST by Hosoda and Kawamura (2004) are also presented

increase from negative to a large positive value ( $>2$  °C) in the same period. After the large  $\Delta$ SST event, high  $SSTA_{LMT6,1m}$  would cause the negative air–sea temperature difference, which suggests that the lowest atmosphere was vertically unstable. This would help to accelerate the SSW through the vertical transfer of the momentum in the atmospheric boundary layer (Wallace et al. 1989). Since appropriate conditions for generating a large  $\Delta$ SST would be impeded by the increased SSW,  $\Delta$ SST would be suppressed over subsequent dates after the large  $\Delta$ SST event. The negative feedback would be inherent in the  $\Delta$ SST mechanism, resulting in extremely short temporal scales of  $\Delta$ SST derived in this study.

## 5 Summary and discussion

Spatial and temporal scales of day-to-day variations for daily-minimum and diurnal SST amplitude were estimated from cloud-free microwave remote sensing observations. By employing a regression scheme using solar radiation and SSW data, global data with high coverage were used in the estimation. The daily-minimum SST anomaly,  $SSTA_{LMT6,1m}$ , was defined as an anomaly from the long-period (seasonal and interannual) component of SST. The diurnal SST amplitude was derived as the afternoon-to dawn (LMT13:00–LMT6:00) SST difference.

Table 1 gives the summary of the derived spatial and temporal scales of this study. Anisotropy of the daily-minimum SST anomaly was not large with spatial scales of  $O(150\text{--}400\text{ km})$ , while the zonal scales of the diurnal SST amplitudes were much larger (up to 1000 km) than their meridional scale [ $O(100\text{--}200\text{ km})$ ]. As shown in Fig. 1, the high diurnal SST amplitudes are associated with atmospheric pressure ridges, where strong solar radiation and weak SSWs form synchronously. The longer zonal scales of diurnal SST are also found at tropics.

Temporal scales of the diurnal SST amplitude and the daily-minimum SST anomaly differ: the former is less than 1 day, while several days of the latter were derived. Therefore, high diurnal SST variation is not persistent at a

geographic point. The composite analysis of satellite observations and atmospheric reanalysis data suggests that high diurnal SSTs have a negative feedback system in which a high diurnal SST change could alter the local conditions by creating atmospheric instability.

As one of the new daily-step SST data sets, one of the advantages in the daily-minimum SST data sets is the high correspondence expected with the subsurface ocean horizontal structures, compared to the daily-mean SST data sets. On the other hand, recent studies have pointed out that the diurnal cycle of SST could modulate the air–sea interaction on intraseasonal (Shinoda and Hendon 1998; Barnie et al. 2005) to decadal temporal scales (Danabasoglu et al. 2006). In addition, by including diurnal cycles air–sea coupled modes in numerical simulations could be improved over wide temporal scales from the MJO (Woolnough et al. 2007; Barnie et al. 2008) to the El-Niño Southern Oscillation (Danabasoglu et al. 2006). To improve geophysical knowledge, atmosphere–ocean studies and numerical predictions of weather and climate will require daily-step data sets of not only the daily-minimum SST, but also the difference between daily maximum and minimum SST estimated from satellite remote sensing.

The day-to-day changes of the daily-minimum SST anomaly have a longer temporal scale [ $O(\text{several days})$ ]. The three-dimensional (spatial–temporal) optimal interpolation would be effective in the production of daily-minimum SST data sets. This is in contrast to estimation using daily-mean SST (Hosoda and Kawamura 2004), in which the temporal scales of daily-mean SST are  $O(1\text{--}2\text{ days})$ , and 3 days at most. The temporal scales of daily-mean SST are shortened in summer, which could be influenced by the diurnal SST variation with extremely short time scales. For checking the influence of diurnal SST cycle on the short temporal scales in the daily-mean SST, moored buoy data were used. The Kuroshio Extension Observatory (KEO) buoy is located south of the Kuroshio Extension at  $32.3^\circ\text{N}$ ,  $144.6^\circ\text{E}$  by the Pacific Marine Environmental Laboratory (PMEL) in the National Oceanic and Atmospheric Administration (NOAA; Cronin et al. 2008). The SST data are obtained by the KEO buoy with 10 min interval. The accuracy of



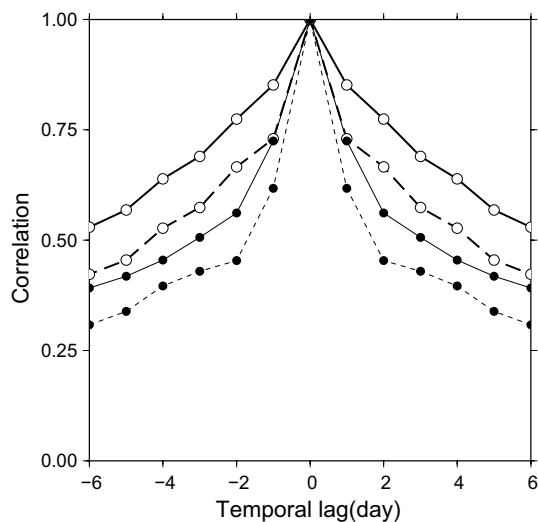


**Fig. 13** Temporal lag correlations derived from the Kuroshio Extension Observatory (KEO) buoy SST time series in June. The 10-min interval SST data from 2004 to 2010, with several data gaps, were used for the calculations. *Heavy lines* correlations using daily-minimum SST around local time 6:00, and *thin lines* correlations using daily-mean SST from local time 0:00 to 24:00. The *broken lines* denote the correlation derived from time series with random noise (amplitude = 0.7 °C) for comparison with satellite SST measurements. Before processing, interannual and seasonal variations of these SST were extracted using Eq. (9)

temperature sensors mounted on the KEO buoy is  $\pm 0.02$  °C ([http://www.pmel.noaa.gov/keo/sensors\\_keo.html](http://www.pmel.noaa.gov/keo/sensors_keo.html)). The data from 2004 to 2010 were used in this study. There were several data gaps in the period due to sensor errors and failure in the mooring. The daily-mean SST and the daily-minimum SST around local mean time 6:00 were calculated from the high-temporal-resolution data. The same method as in Sect. 3.1, used for extracting short-term signal using a low-pass filter [Eq. (9)], was applied to these time series and temporal lag-correlation was calculated. For comparing the satellite remote sensing of SST, time series with adding random noise of 0.7 °C amplitude were also examined. From validation results of satellite SST data (Hosoda 2013), the amplitude of random noise on time series was determined. Figure 13 shows an example of temporal lag correlation functions derived from June data. Using the daily-mean SST data, the correlations decreased rapidly to 0.5 within  $\pm 3$ -day lag. On the other hand, the high correlations ( $>0.5$ ) were persistent over up to  $\pm 9$  days from the daily-minimum SST data. This means that the temporal scales from the daily-minimum SST would be twice or triple those from the daily-mean SST. The difference between them is that the daily-mean SST data include the diurnal variation at each date, whose amplitudes are changeable in day-to-day time series, as described in this study. Then it can be concluded that the shorter time scales in daily-mean SST (Hosoda and

Kawamura 2004), especially in summertime, were affected by day-to-day change of the diurnal SST variations. The longer temporal scales [ $O(9\text{--}10$  days) for the daily-minimum SST] derived from in situ data might be owing to the higher sensor accuracy compared to satellite remote sensing. From the noise-added daily-mean SST time series, the temporal-lag correlations were lower than 0.5, except for adjacent dates. While the temporal-lag correlations from noise-added daily-minimum SST likewise decreased, they were above 0.5 even at  $\pm 4$ -day lag. This result suggests that the diurnal correction would enable the three-dimensional (zonal/meridional/temporal) optimal interpolation to reproduce realistic SST fields.

The derived spatial-temporal scales for daily-minimum SST were complementary to each other. In high EKE areas, where mesoscale disturbances are frequently generated, the spatial scales are as short as 100–300 km, while the temporal scales are longer than 4 days. On the other hand, short temporal scales are often located in low EKE areas, where long spatial scales have occurred. It is possible that, in the former, optimal interpolation with high weighting in the temporal direction could reasonably approximate the SSTA fields with fine spatial structure. For the latter, transient SST phenomena over a wide coverage could be reproduced by the optimal interpolation with high weighting in the spatial direction. Since this analysis reveals that these SST variations are dominant in each area and season, the optimal interpolation using the derived decorrelation scales is expected to produce realistic SST fields. The UK Met Office and Remote Sensing Systems have already produced diurnal-free SST data sets, as operational sea surface temperature and sea ice analysis (OSTIA; Donlon et al. 2011) and microwave-infrared optimally interpolated daily sea surface temperatures (MW-IR OI SST; <http://www.remss.com/node/5132>), respectively. The next target of our studies is to produce a gridded daily-minimum SST data set employing the decorrelation scales derived here, which is expected to provide a possible measure for foundation SST.

This study focused on diurnal warming phenomena, and removed them by an empirically method. The correction method used in this study was based on the daily-mean solar radiation and simultaneous observation of SSW by microwave radiometers. Actually, these weather parameters could also show diurnal variation by air–sea interaction. Evaporation from sea surface caused by solar heating could generate clouds by diurnally varying atmospheric convection, which could affect cloudiness. The vertical unstable condition over extremely high diurnal SST warming in the atmospheric boundary layer could also cause vertical mixing of atmospheric momentum within a day, destroying the diurnal SST warming condition. In addition, diurnal variations of sea-water transparency, which could be induced by phytoplankton blooms, also have the potential to affect the

SST variation, since the sea-water transparency changes the vertical distribution of solar heating in upper ocean layer. On the other hand, diurnal SST cooling phenomena under various ocean heat loss conditions would be also dependent on weather and oceanic variability. These phenomena will be studied in the future by using ultra-high temporal resolution data by geostationary satellites or appropriate numerical models.

**Acknowledgments** The author would like to express gratitude to members of physical oceanographic and satellite oceanographic groups in Tohoku University for their helpful comments and advice. Two anonymous reviewers and the editor gave valuable comments and suggestions for improving the manuscript. The Japan Aerospace Exploration Agency (JAXA) provided SST and SSW data by the AMSR-E and JASMES (JAXA Satellite Monitoring for Environmental Studies) radiation data. The SST and SSW observations by Windsat were released by the Remote Sensing Systems. The Kuroshio Extension Observatory (KEO) buoy data were provided by the National Oceanic and Atmospheric Administration/Pacific Marine Environmental Laboratory (NOAA/PMEL). The Global Modeling and Assimilation Office (GMAO) and the GES DISC are thanked for the dissemination of Modern-era Retrospective-analysis for Research and Applications (MERRA) heat flux data.

### Appendix: Local times of daily-minimum and maximum SST and variability

This section describes the validity of the assumption that the SST at LMT6:00/LMT13:00 at 1 m depth ( $SST_{LMT6,1m}/SST_{LMT13,1m}$ ) is the daily-minimum/daily-maximum SSTs at 1-m depth. Hosoda (2013) made a choice of those for reference times since the AMSR-E ascending [local time of ascending node (LTAN): 13:30] and Windsat descending [local time of descending node (LTDN): 6:00] were close to these local times. Using in situ SST measurements by drifting and moored buoys, these assumptions were evaluated. Surface marine data from the buoys were gathered by the Global Telecommunications System (GTS). GTS data are available from National Centers for Environmental Prediction (NCEP) of the NOAA and Canadian Marine Environmental Data Service (MEDS). The SST sensors on buoys are calibrated to an accuracy of  $\pm 0.1$  °C before they are deployed to the ocean (Sybrandy et al. 2009).

The quality control process described in Hosoda and Qin (2011) was applied to remove anomalous buoy observations. Buoy data with at least hourly resolution were used for this analysis. The period analyzed is from 2002 to 2011. The number of total data in this analysis is 708,249.

Figure 14 shows a histogram of the local time at which the daily minimum SSTs were observed by buoys. In every season and in both hemispheres, the maximum frequency was found at LMT6:00. This feature was emphasized in

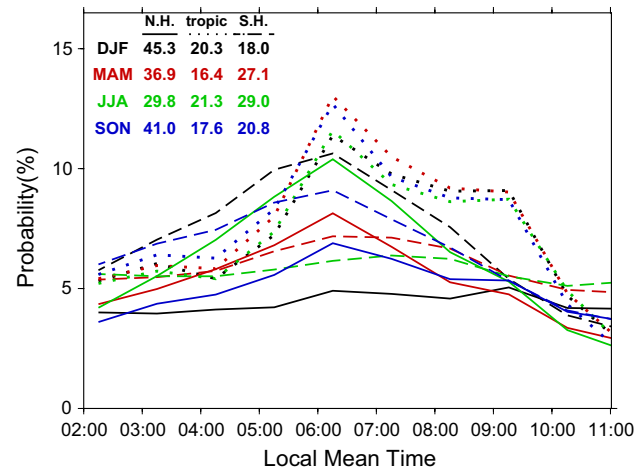


**Fig. 14** Seasonal histograms of local mean time at which drifting buoys observed the daily minimum SST in the morning. Color texts and numbers at the upper left denote the months for calculating respective colored histograms and the probabilities of dates without significant minimum SST record (i.e., SST variation in the analyzed local time was less than 0.1 °C). The solid and dashed lines were obtained from the extra-tropical North (20–60°N) and South Hemispheres (20–60°), respectively. Dotted lines were calculated in the tropical oceans (20°S–20°N)

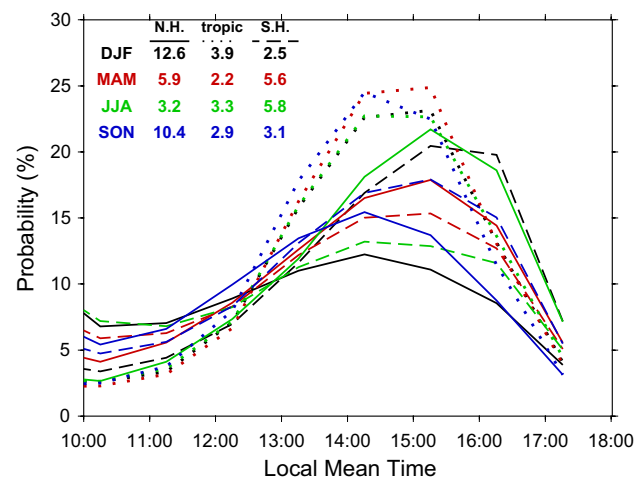


**Fig. 15** Same as Fig. 14, but for daily-maximum SST around the local noon time

the warming-up seasons (spring and summer), when the diurnal amplitudes were intensive (Fig. 2). Fifty percent or more of the observed daily minimum SSTs were included in the range of LMT6:00  $\pm$  2 h (i.e., LMT4:00–LMT8:00).

A histogram for the daily-maximum SST is provided in Fig. 15. Broad peaks were found in the range of LMT13:00–LMT16:00. In the cooling seasons that consist of October–March (April–September) in the Northern (Southern) Hemisphere, the frequencies in the early afternoon (LMT13:00–LMT14:00) are slightly larger. In the

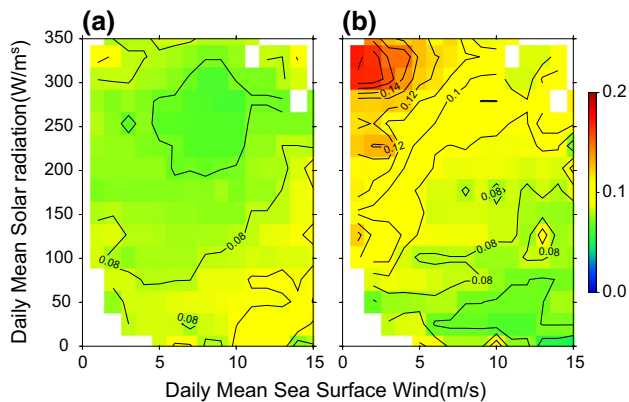


**Fig. 16** Buoy observed sea surface temperature (SST) dependency on the daily-mean sea surface wind (SSW) and solar radiation (SR). (a, b) SST fluctuations during the morning (LMT3:00–LMT9:00) and afternoon (LMT13:00–LMT17:00), respectively. The SST fluctuations were defined as the average in a box ( $SSW/SR = 1 \text{ ms}^{-1}/20 \text{ Wm}^{-2}$ ) of max–min differences in the respective local mean time observed by each buoy. Contour intervals are  $0.1 \text{ }^{\circ}\text{C}$

warming seasons, the peaks shift toward late afternoon (LMT15:00–LMT16:00).

The SST variations in the morning (LMT3:00–LMT9:00) and afternoon (LMT13:00–LMT17:00) are shown in Fig. 16, which depicts the box averages of the SST ranges between the highest and the lowest for each buoy in the respective temporal period. In the morning, the SST variations were less than  $0.1 \text{ }^{\circ}\text{C}$ , which indicates that the SST changes were smaller than the buoy sensors' accuracy. Therefore, the SST at LMT6:00 could be one of the representatives for the daily-minimum SST, as defined in this study. However, the SST variations in the afternoon were larger than  $0.1 \text{ }^{\circ}\text{C}$  in the range of high diurnal SST change. It is possible that the diurnal amplitudes defined in this study are under-estimated as great as  $0.2 \text{ }^{\circ}\text{C}$ , which are, however, significantly less than microwave sensors' accuracy [e.g., Noise Equivalent Differential Temperature ( $ND\Delta T$ ) =  $0.3 \text{ K}$  for AMSR-E 6 GHz channel; Kawanishi et al. 2003]. Improving the estimation method of the diurnal SST amplitude will be discussed in a future study.

## References

- Barnie DJ, Woolnough SJ, Slingo JM, Guilyardi E (2005) Modeling diurnal and intraseasonal variability of the ocean mixed layer. *J Clim* 18:1190–1202
- Barnie DJ, Guilyardi E, Madec G, Slingo JM, Woolnough SJ, Cole J (2008) Impact of resolving the diurnal cycle in an ocean-atmosphere GCM. Part 2: a diurnally coupled CGCM. *Clim Dyn* 31:909–925. doi:10.1007/s00382-008-04290z
- Chelton DB, Wentz FJ, Gentemann CL, de Szoeko RA, Shlax MG (2000) Satellite microwave SST observations of transequatorial tropical instability waves. *Geophys Res Lett* 27:1239–1242
- Cronin MF, Meinig C, Sabine CL, Ichikawa H, Tomita H (2008) Surface mooring network in the Kuroshio Extension. *IEEE Syst J* 2:424–430
- Danabasoglu G, Large WG, Tribbia JJ, Briegleb PRGBP (2006) Diurnal coupling in the tropical oceans of CCSM3. *J Clim* 19:2347–2365
- de Souza RB, Mata MM, Garcia CAE, Kampel M, Oliveira EN, Lorenzetti JA (2006) Multi-sensor satellite and in situ measurements of a warm core ocean eddy south of the Brazil–Malvinas Confluence region. *Remote Sens Environ* 100:52–66
- Dong C, Nencioli F, Liu Y, McWilliams JC (2011) An automated approach to detect oceanic eddies from satellite remotely sensed sea surface temperature data. *IEEE Geosci Remote Sens* 8:1055–1059
- Donlon C, Robinson I, Casey KS, Vazquez-Cuervo J, Armstrong E, Arino O, Gentemann CL, May D, LeBorgne P, Piollé J, Barton I, Beggs H, Poulter DJS, Merchant CJ, Bingham A, Heinz S, Harris A, Wick G, Emery B, Minnett P, Evans R, Llewellyn-Jones D, Mutlow C, Reynolds RW, Kawamura H, Rayner N (2007) The global ocean data assimilation experiment high-resolution sea surface temperature pilot project. *Bull Am. Meteorol Soc* 88:1197–1213
- Donlon CJ, Martin M, Stark J, Roberts-Jones J, Fiedler E, Wimmer W (2011) The operational sea surface temperature and sea ice analysis (OSTIA) system. *Remote Sens Environ* 116:140–158
- Emery WJ, Thomson RE (2001) Data analysis methods in physical oceanography, 2nd edn. Elsevier Science, Amsterdam, p 640
- Hasegawa T, Yasuda T, Hanawa K (2007) Generation mechanism of quasidecadal variability of upper ocean heat content in the equatorial Pacific Ocean. *J Geophys Res* 112:C0812. doi:10.1029/2006JC003755
- Hosoda K (2011) Algorithm for estimating sea surface temperatures based on Aqua/MODIS global ocean data. 2. Automated quality check process for eliminating cloud contamination. *J Oceanogr* 67:791–805. doi:10.1007/s10872-011-0077-5
- Hosoda K (2012) Local phase relationship between sea surface temperature and net heat flux over weekly to annual periods in the extratropical North Pacific. *J Oceanogr* 68:671–685. doi:10.1007/s10872-012-0127-7
- Hosoda K, Kawamura H, Lan K-W, Shimada T, Sakaida F (2012) Temporal scale of sea surface temperature fronts revealed by microwave observations. *IEEE Geosci Remote Sens Lett* 9:3–7. doi:10.1109/LGRS.2011.2158512
- Hosoda K (2013) Empirical method of diurnal correction for estimating sea surface temperature at dawn and noon. *J Oceanogr* 69:631–646. doi:10.1007/s10872-013-0194-4
- Hosoda K, Kawamura H (2004) Global space-time statistics of sea surface temperature estimated from AMSR-E data. *Geophys Res Lett* 31. doi:10.1029/2004GL020317
- Hosoda K, Qin H (2011) Algorithm for estimating sea surface temperatures based on Aqua/MODIS global ocean data. 1. Development and validation of the algorithm. *J Oceanogr* 67:135–145. doi:10.1007/s10872-011-0007-6
- Hu C, Muller-Karger F, Murch B, Myhre D, Taylor J, Luerssen R, Moses C, Zhang C, Gramer L, Hendee K (2009) Building an automated integrated observing system to detect sea surface temperature anomaly events in the Florida Keys. *IEEE Trans Geosci Remote Sens* 47:1607–1620. doi:10.1109/TGRS.2008.2007425
- Kawai Y, Kawamura H (2002) Evaluation of the diurnal warming of sea surface temperature using satellite-derived marine meteorological data. *J Oceanogr* 58:805–814
- Kawai Y, Wada A (2007) Diurnal sea surface temperature variation and its impact on the atmosphere and ocean: a review. *J Oceanogr* 63:721–744
- Kawanishi T, Sezai T, Ito Y, Imaoka K, Ishida Y, Shibata A, Miura M, Inahata H, Spencer RW (2003) The Advanced Microwave



- Scanning Radiometer for the Earth Observing System (AMSR-E), NASA's contribution to EOS for global energy and water cycle studies. *IEEE Trans Geosci Remote Sens* 41:184–194
- Kennedy JJ, Brohan P, Tett SFB (2007) A global climatology of the diurnal variations in sea surface temperature and implications for MSU temperature trends. *Geophys Res Lett* 34:L05712. doi: [10.1029/2006GL028920](https://doi.org/10.1029/2006GL028920)
- Kuragano T, Kamachi M (2000) Global statistical space-time scales of oceanic variability estimated from the TOPEX/POSEIDON altimeter data. *J Geophys Res* 105:955–974
- Kurihara Y, Sakurai T, Kuragano T (2006) Global daily sea surface temperature analysis using data from satellite microwave radiometer, satellite infrared radiometer and in-situ observations. *Weather Bull JMA* 73:s1–s18 (in Japanese)
- Lan K-W, Kawamura H, Lee M-A, Lu H-J, Shimada T, Hosoda K, Sakaida F (2012) Relationship between albacore (*Thunnus alalunga*) fishing grounds in the Indian Ocean and the thermal environment revealed by cloud-free microwave sea surface temperature. *Fish Res* 113:1–7
- Le Traon P-Y, Nadal F, Ducet N (1998) An improved mapping method of multisatellite altimeter data. *J Atmos Oceanic Technol* 15:522–534
- Provost C, Garcia O, Garcon V (1992) Analysis of satellite sea surface temperature time series in the Brazil–Malvinus Current Confluence region: Dominance of the annual and semiannual periods. *J Geophys Res* 97:17841–17858
- Qin H, Kawamura H, Kawai Y (2007) Detection of hot event in the equatorial Indo-Pacific warm pool using advanced satellite sea surface temperature, solar radiation, and wind speed. *J Geophys Res* 112:C07015. doi: [10.1029/2006JC003969](https://doi.org/10.1029/2006JC003969)
- Reynolds RW, Smith TM, Liu C, Casey DBCKS, Schlax MG (2007) Daily high-resolution-blended analyses for sea surface temperature. *J Clim* 20:5473–5496
- Reynolds RW, Smith TM (1994) Improved global sea surface temperature analyses using optimum interpolation. *J Clim* 7:929–949
- Rienecker MM, Suarez MJ, Gelaro R, Todling R, Bacmeister J, Liu E, Bosilovich MG, Schubert SD, Takacs L, Kim G-K, Bloom S, Chen J, Collins D, Conaty A, da Silva A, Gu W, Joiner J, Koster RD, Lucchesi R, Molod A, Owens T, Pawson S, Redder PPCR, Reichle R, Robertson FR, Ruddick AG, Sienkeiwicz M, Woollen J (2011) MERRA: NASA's modern-era retrospective analysis for research and applications. *J Clim* 24:3624–3648
- Rodwell MJ, Hoskins BJ (2001) Subtropical anticyclones and summer monsoons. *J Clim* 14:3192–3211
- Shinoda T, Hendon H (1998) Mixed layer modeling of intra-seasonal variability in the tropical western Pacific and Indian Oceans. *J Clim* 11:2668–2685
- Sugimoto S, Hanawa K (2011) Roles of SST anomalies on the winter-time turbulent heat fluxes in the Kuroshio-Oyashio Confluence Region: influence of warm eddies detached from the Kuroshio Extension. *J Clim* 24:6551–6561. doi: [10.1175/2011JCL14023.1](https://doi.org/10.1175/2011JCL14023.1)
- Sybrandy WAL, Niiler PP, Martin C, Scuba W, Charpentier E, Meldrum DT (2009) Global Drifter programme barometer drifter design reference. Technical report, Data Buoy Cooperation Panel Technical Document No.4, revision 2.2
- Trenberth KE (1991) Storm tracks in the Southern Hemisphere. *J Atmos Res* 48:2159–2178
- Wallace JM, Mitchell TP, Deser C (1989) The influence of sea-surface temperature on surface wind in the Eastern Equatorial Pacific: seasonal and interannual variability. *J Clim* 2:1492–1499
- White WB (1995) Design of global observing system for gyre-scale upper ocean temperature variability. *Prog Oceanogr* 36:169–217
- Woolnough SJ, Vitart F, Balmaseda MA (2007) The role of the ocean in the Madden–Julian Oscillation: implications for MJO prediction. *Q J R Meteorol Soc* 133:117–128. doi: [10.1002/qj.4](https://doi.org/10.1002/qj.4)
- Yashayaev IM, Zveryaev II (2001) Climate of the seasonal cycle in the North Pacific and the North Atlantic Oceans. *Int J Climatol* 21:401–417. doi: [10.1002/joc.585](https://doi.org/10.1002/joc.585)
- Zainuddin M, Kiyofuji H, Saitoh K, Saitoh S-I (2006) Using multi-sensor satellite remote sensing and catch data to detect ocean hot spots for albacore (*Thunnus alalunga*) in the northwestern North Pacific. *Deep-Sea Res* 53:419–431